Methane Oxygenation Hot Paper

How to cite: Angew. Chem. Int. Ed. 2021, 60, 8889–8895
International Edition: doi.org/10.1002/anie.202016888
German Edition: doi.org/10.1002/ange.202016888

Fe/Fe_3C Boosts H_2O_2 Utilization for Methane Conversion Overwhelming O_2 Generation

Yicheng Xing, Zheng Yao, Wenyuan Li, Wenting Wu, Xiaoqing Lu, Jun Tian, Zhongtao Li, Han Hu, and Mingbo Wu**

Abstract: *H_2O_2 as a well-known efficient oxidant is widely used in the chemical industry mainly because of its homolytic cleavage into $^{\bullet}OH$ (stronger oxidant), but this reaction always competes with O_2 generation resulting in H_2O_2 waste. Here, we fabricate heterogeneous Fenton-type Fe-based catalysts containing Fe-N_x sites and Fe/Fe_3C nanoparticles as a model to study this competition. Fe-N_x in the low spin state provides the active site for $^{\bullet}OH$ generation. Fe/Fe_3C, in particular Fe_3C, promotes Fe-N_x sites for the homolytic cleavages of H_2O_2 into $^{\bullet}OH$, but Fe/Fe_3C nanoparticles (Fe^0 as the main component) with more electrons are prone to the undesired O_2 generation. With a catalyst benefiting from finely tuned active sites, 18% conversion rate for the selective oxidation of methane was achieved with about 96% selectivity for liquid oxygenates (formic acid selectivity over 90%). Importantly, O_2 generation was suppressed 68%. This work provides guidance for the efficient utilization of H_2O_2 in the chemical industry.*

Introduction

H_2O_2, a well-known efficient and environmentally friendly oxidant, has been regarded as one of the 100 most important chemicals in the world due to its wide applications especially in chemical synthesis.[1] However, the excess H_2O_2, great deviation in product composition from the stoichiometry, are always involved in these reactions, which greatly raise production costs and decrease the product yield and selectivity. Actually, O_2 evolution always competitively accompanied with H_2O_2 itself utilization or the homolytic cleavage of H_2O_2 to generate $^{\bullet}OH$ (stronger oxidant), but this competitive process is ignored. Like iron porphyrin, there is a general and ambiguous agreement that heterogeneous Fe-based catalysts containing Fe-N_x structure can act as Photo-Fenton catalyst for the reaction in the presence of H_2O_2.[2] However, up to now, almost no clear evidence or investigation was discussed in detail about the influence of various other Fe species (unavoidable species when large-scale preparation) in Fe-N_x based catalysts for H_2O_2 decomposition.

As the main component of extremely abundant natural gas and shale gas, methane is an economical chemical feedstock to be converted into its oxygenated derivatives, easily transportable and storable liquid chemicals.[3] Traditionally, it is an energy-intensive and indirect way to its industrials synthesis that entails such as steam-reforming and subsequent Fischer–Tropsch synthesis.[4] The direct selective oxidation of methane to oxygenates is more attractive but remains great challenges because of methane's high C–H bond strength (439.3 kJ mol^{-1}), negligible electron affinity, and low polarizability.[5] Furthermore, the value-added oxygenates such as methanol, formaldehyde and formic acid are more active than methane molecules and are prone to deep mineralization.[6] Among various activating reagents of methane, hydroxyl radicals ($^{\bullet}OH$), mainly from H_2O_2 decomposition, is green and mild to achieve C–H bond cleavage. Hutchings et al.[7] utilize H_2O_2 and O_2 to oxidize CH_4 into methanol using Au-Pd colloidal catalysts, resulting in methanol selectivity of around 73% (a total organic compound selectivity of 92%). Deng et al.[8] reported that inexpensive catalyst containing graphene-confined single iron atoms can convert CH_4 to C1 oxygenated mixture (CH_3OH, CH_3OOH, $HOCH_2OOH$ and HCOOH) using H_2O_2 as an oxidant, and the highest selectivity of the total C1 oxygenated products was around 94% (selectivity of CH_3OOH, 34%; selectivity of HCOOH, 29%). Therefore, the selective oxidation of methane was selected as the model reaction to study in this work, because there is still great challenge in developing highly active and inexpensive catalysts to efficient utilize H_2O_2 in this selective oxidation reaction.

Herein, we fabricate a model catalyst, that is FeN_x/C catalyst with Fe-N_x sites and graphene-encapsulated Fe/Fe_3C nanoparticles through a one-step pyrolysis, and these active sites were finely tuned via Fe-imidazole coordination compound (Fe-ZIF, Fe source) and melamine (N source to stabilize Fe atom and to balance Fe content) under different temperature. These catalysts were used in the direct methane conversion into oxygenated products with the presence of H_2O_2 at mild condition (room temperature and atmospheric pressure). The methane conversion rate of optimized catalyst

[*] Y. Xing, Z. Yao, W. Li, Prof. W. Wu, Z. Li, H. Hu, Prof. M. Wu
State Key Laboratory of Heavy Oil Processing
Institute of New Energy, College of Chemical Engineering
China University of Petroleum (East China)
Qingdao 266580 (P. R. China)
E-mail: wuwt@upc.edu.cn
wumb@upc.edu.cn

Prof. X. Lu
College of Materials Science and Engineering
China University of Petroleum (East China)
Qingdao 266580 (P. R. China)

Prof. J. Tian
State Key Laboratory of Molecular Engineering of Polymers and Department of Macromolecular Science, Fudan University
Shanghai 200433 (P. R. China)

Supporting information and the ORCID identification number(s) for the author(s) of this article can be found under: https://doi.org/10.1002/anie.202016888.

(FeN_x/C-5-700) can reach 18% with a liquid oxygenates selectivity of about 96% (formic acid selectivity over 90%, 4659 μmol g_{cat}^{-1}). At the same time, the O_2 generation was suppressed 68%, greatly reducing H_2O_2 waste. Through a series of characterization methods, it shows that Fe-N_x is essential to $^{\bullet}OH$ generation for further methane conversion, and proper Fe/Fe_3C nanoparticles can dramatically facilitate this process due to its good electron transport ability. However, further tuning various Fe species make catalyst processing more electrons, which in turn promote the O_2 generation and overwhelm $^{\bullet}OH$ generation. This finding provides guidance for the rational design catalysts to efficiently utilize H_2O_2 and its application in selective oxidation reactions.

Results and Discussion

The synthesis of FeN_x/C-R-T (R represents the mass ratio of melamine over Fe-ZIF, T represents the pyrolysis temperature.) were carried out via a one-step pyrolysis of Fe precursors and melamine (See Supporting Information for the details). R at 5 was selected in this work according to their catalytic performance (vide infra). In order to study the roles of various Fe species, T at 600, 700 and 800 °C were selected to prepare the catalysts. Chemical structures of this series of FeN_x/C-R-T were first characterized by X-ray diffraction (XRD, Figure S1). For FeN_x/C-5-800, the primary diffraction peak at 26.1° can be assigned to (002) planes of graphitic carbon. And five diffraction peaks at 37.7°, 42.8°, 43.7°, 45.8° and 44.6° in the XRD pattern of FeN_x/C-5-800 can be attributed to (210), (211), (102), (112) planes of Fe_3C (cohenite, JCPDS No. 35-0772), and (110) planes of cubic Fe (JCPDS No. 06-0696), respectively. When reducing the synthesis temperature to 700 °C, weak broad peaks can be observed at relative positions (FWHM, full width at half maximum, Table S1). It indicates that the content of Fe/Fe_3C nanoparticles decrease as reducing pyrolysis temperature. For FeN_x/C-5-600, there is almost no peaks from 35° to 70°, indicating that there is little Fe/Fe_3C species.

The transmission electron microscopy (TEM) images of FeN_x/C-5-600 (Figure 1a) show that it has a distinct layered porous structure. Fe, N and C elements were further identified and mapped out by Energy dispersive X-ray spectrometer (EDS) (Figure 1b). The C and N elements are uniformly distributed and the overlay of Fe and N signals in the elemental mapping images (Figure 1c) clearly discloses that Fe atoms are adjacent to N atoms at atomic level, suggesting the presence of Fe-N_x coordination (Figure 1d). As the pyrolysis temperature increases (700 °C), Fe/Fe_3C nanoparti-

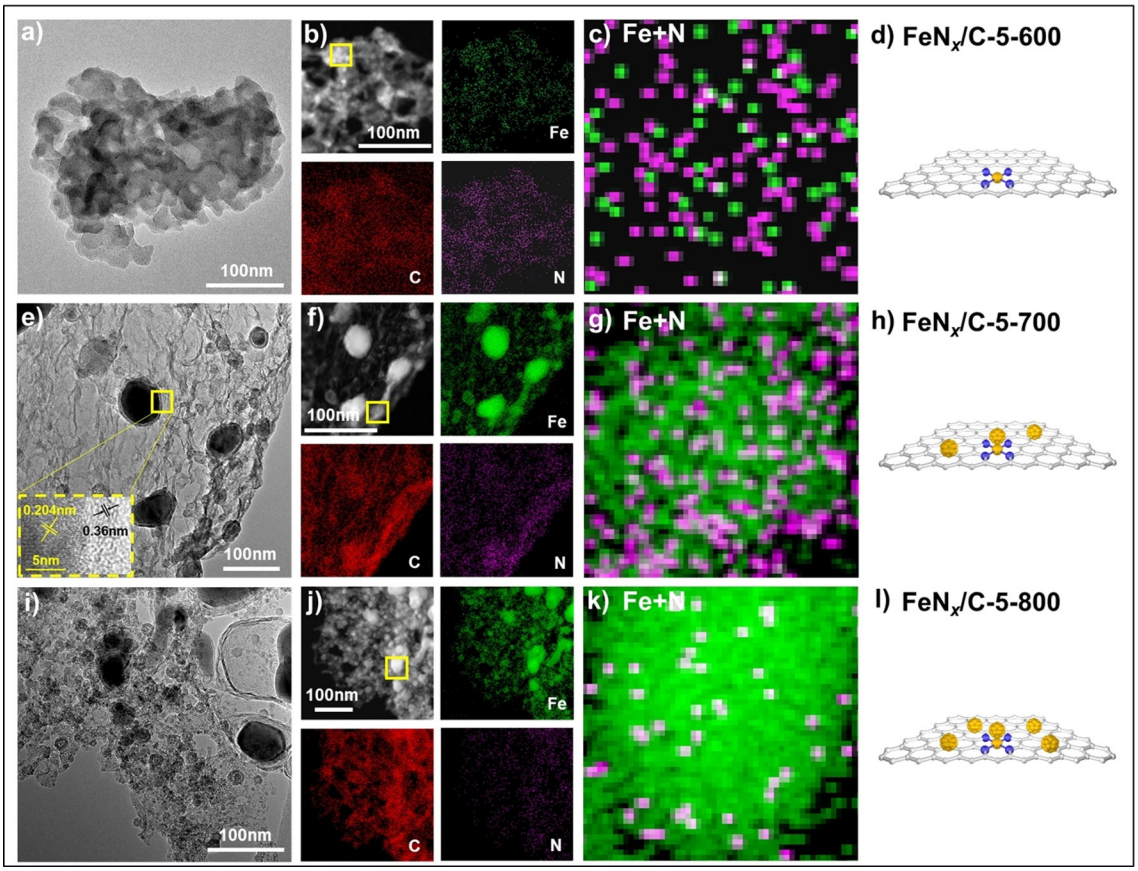

Figure 1. a) TEM images, b,c) HADDF-STEM EDS mapping, d) schematic illustration of model systems of FeN_x/C-5-600. e) TEM images, f,g) HADDF-STEM EDS mapping, h) schematic illustration of model systems of FeN_x/C-5-700. i) TEM images, j,k) HADDF-STEM EDS mapping, l) schematic illustration of model systems of FeN_x/C-5-800. (c), (g), and (k) are enlarged figures from the yellow square frames in (b), (f) and (j), respectively. Yellow, blue, and white spheres in (d), (h), and (l) depict Fe, N, and C atoms, respectively.

cles with a lattice distance of 0.204 nm (the *d*-spacing of (110) planes of α-Fe or (220) planes of Fe_3C) are encapsulated with well crystallized graphene layers (lattice distance of 0.36 nm) (Figure 1 e), and these graphite may stabilize the nanoparticles.[9] EDS of FeN_x/C-5-700 shows that uniformly distributed C and N elements still exist, but some of Fe elements aggregate (Figure 1 f,g), suggesting that there is Fe-N_x coordination and it overlaps with Fe/Fe_3C nanoparticles (Figure 1 h). In addition, as the pyrolysis temperature increases to 800 °C, most Fe seems to aggregate and left more exposed Fe/Fe_3C active sites (Figure 1 i). At the same time, N content reduces obviously, indicating that Fe-N_x sites were reduced and may transformed into the exposed Fe/Fe_3C nanoparticles (Figure 1 j, k, l).

In X-ray photoelectron spectroscopy (XPS) of these FeN_x/C-5-T catalysts (Figure 2 a, S2 and S3), signals corresponding to the elements Fe, C, N, O and almost no S are observed in the wide spectrum survey. The Fe content of these samples increases as the temperature increase from 600 to 800 °C (Table S2). The signal at around 711 eV can be assigned to Fe in Fe-N_x configuration, which can be observed in all catalysts.[10] The signal at 707.1 eV in Fe 2p spectra of FeN_x/C-5-700 and FeN_x/C-5-800 can be assigned to zero-valance Fe (metallic iron or carbide).[11] The N content shows the opposite trend (Table S3), and it decreases from 46.9 % (FeN_x/C-5-600) to 5.5 % (FeN_x/C-5-800), which are consistent with STEM results.

In order to further reveal the structure-property relationship of these catalysts, X-ray absorption spectroscopy at Fe K-edge was further conducted to analyze the valence states and coordination environment of Fe species (Figure 2 b). As shown in Fe K-edge XANES (dipole transition from 1s to 4p),[12] Fe K-edge spectrum of FeN_x/C-5-600 is close to that of Fe(TPPCl)(II), suggesting that its valance state is close to Fe^{II} divalent state. The absorption edge of FeN_x/C-5-700 shifts to lower energy, indicating that the valence state of Fe species in FeN_x/C-5-700 is lower than Fe^{II} divalent state. Associated with TEM and XPS, it is probably because of the increasing content of Fe/Fe_3C nanoparticles, resulting in the higher electron density than that of FeN_x/C-5-600. Similarly, FeN_x/C-5-800 processing the lowest energy among these catalysts, means that it has the highest electron density among these catalysts.

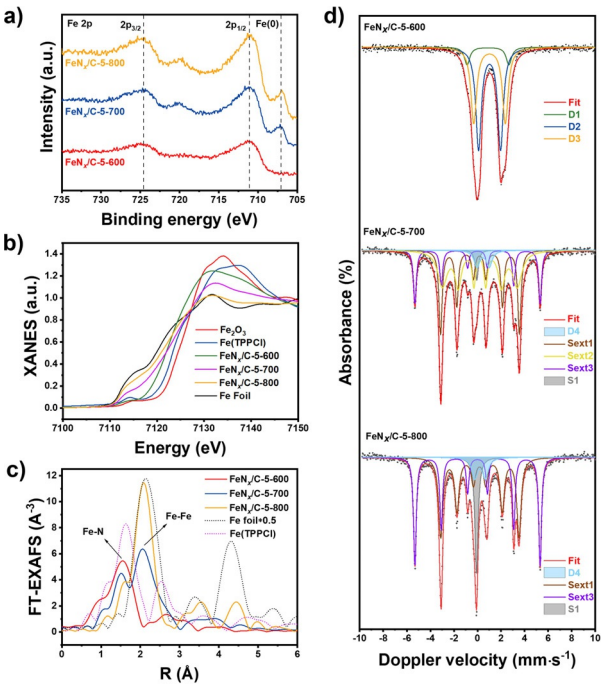

Figure 2. a) Fe 2p XPS spectra of FeN_x/C-5-T. b) K-edge XANES spectra of FeN_x/C-5-T, Fe foil, Fe_2O_3, Fe(TPPCl). c) Fourier transforms of the k^3-weighted K-edge EXAFS spectra of FeN_x/C-5-T, Fe foil, Fe(TPPCl). d) ^{57}Fe Mössbauer spectra of FeN_x/C-5-T.

The k^3-weighted Fourier transformation of Fe K-edge from extended X-ray absorption fine structure (EXAFS) spectra for these catalysts were further studied as shown in Figure 2 c, and the relative fitting results were summarized in Table S4. For FeN_x/C-5-600, the first shell peaks at around 1.45 Å can be assigned to Fe-N, confirming the existence of Fe-N_4.[13] For FeN_x/C-5-700, it shows a strong peak around 2.09 Å, which can be attributed to Fe-Fe shell. There is a shoulder peak around 2.70 Å, which may be assigned to Fe-C shell. Compared with FeN_x/C-5-700, FeN_x/C-5-800 show a sharp and strong peak at around 2.09 Å. It can be seen that the intensity of Fe-Fe shell in R space increases and Fe-N_x reduces as increasing the pyrolysis temperature (Figure 2 c). The Fe-Fe coordination number increases from 1.9 (FeN_x/C-5-700) to 5.5 (FeN_x/C-5-800). Combined with the STEM results, it can be inferred that Fe-N_x sites overlap with Fe/Fe_3C nanoparticles in FeN_x/C-5-700. Further increasing pyrolysis temperature to 800 °C, more accumulated Fe/Fe_3C nanoparticles intensely overlap with the Fe-N_x sites in FeN_x/C-5-800. This overlap structure can promote the increasing electron density of Fe-N_x seizing from Fe/Fe_3C sites.

In order to carefully analysis Fe species function, the contents of various Fe species were further distinguished by Mössbauer spectroscopy (Figure 2 d). The Mössbauer fitting parameters and the relative areas of different Fe species are shown in Table S5. The curve of FeN_x/C-5-600 was fitted to three components. Doublet D1 and D2 are both assigned to high-spin states of Fe^{II}-N_4 coordination. Ferric high spin complexes have relatively small quadrupole splitting values as only the lattice term contributes.[14] D3 can be ascribed to middle-spin states of Fe^{II}-N_4 coordination.[15] The curve of FeN_x/C-5-700 was fitted to five components. Concretely, doublet D4 is assigned to low-spin states of Fe^{II}-N_4 coordination with a relative content of 11.9 %.[16] Sextet 1 and sextet 2 both are assigned to Fe_3C with a total relative content of 68 %.[14] Sextet 3 and singlet 1 are assigned to Fe^0 that is α-Fe and Superparamagnetic Fe, with the total relative content of 20.1 %. The curve of FeN_x/C-5-800 is similar to FeN_x/C-5-700, but the contents of Fe^0 and Fe_3C are different. The total relative contents of Fe^0 and Fe_3C in FeN_x/C-5-800 are 49.9 % and 42.7 %, respectively. Combined with ICP measurements, the content of each Fe species was calculated and listed in Table S6. The Fe-N_x content decreased from 10.9 % (FeN_x/C-5-600) to 1.1 % (FeN_x/C-5-800). FeN_x/C-5-800 has a little more content Fe than that of FeN_x/C-5-700, but FeN_x/C-5-700 has more Fe_3C and less Fe^0, which may cause the electron density FeN_x/C-5-700 lower than that of FeN_x/C-5-800.

In order to study structure-property of catalysts for H_2O_2 assisted catalysis performance, catalysts prepared at different pyrolysis temperature and ratios between metal precursors and melamine in the methane conversion with the assistant of H_2O_2 are carefully studied (Figure 3a, S4, S5 and Table S7).

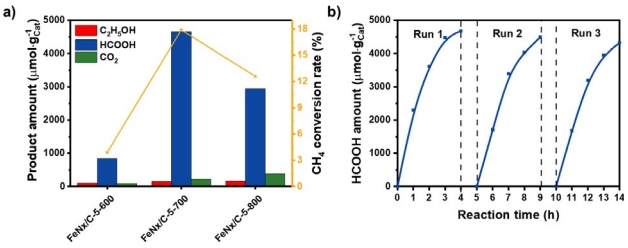

Figure 3. a) Product yields and methane conversion rates of FeN_x/C-5-T. b) Three runs of formic acid production by FeN_x/C-5-700. Reaction conditions: 8 mg catalysts, 1 mL 0.5 M H_2O_2, 4 mL deionized water, 1 atm CH_4, 1500 W m^{-2} Xe lamp, 25 °C, 4 h reaction time.

FeN_x/C-5-700 shows the highest methane conversion (18 %) as the pyrolysis temperature is 700 °C. With the assistant of H_2O_2, formic acid as the main products can reach 4659 μmol g_{cat}^{-1} with over 90 % selectivity, ethanol as the major by-product has around 6 % selectivity, leading to 96 % in total for liquid oxygenates selectivity, and CO_2 as the only gas oxygenates has only 4 % selectivity without CO, hydrocarbons and other liquid oxygenates produced. FeN_x/C-5-800 is second, and the lowest is FeN_x/C-5-600. For the precursor ratio on the catalytic activity, it can be clearly found that the ratio at 5 (FeN_x/C-5-700) greatly benefits the methane conversion. Compared with the previous reports, FeN_x/C-5-700 shows significant higher activity and selectivity for photo- or thermocatalytic direct oxidation of CH_4 with H_2O_2 (Table S8).[7,8,17] In addition, FeN_x/C-5-700 still has good catalytic ability after 3 recycle tests, indicating its excellent stability (Figure 3b). According to the ICP measurements, the content of Fe species was almost unchanged after 3 recycle tests (Table S2). And the XAS reveals that FeN_x/C-5-700 almost retains the same chemical state and coordination after reaction (Figure S6). To further support the above results, Mössbauer spectroscopy were used to distinguish the change of Fe species in FeN_x/C-5-700 and FeN_x/C-5-800 after reaction (Figure S7). The Mössbauer fitting parameters as well as the relative areas of various Fe species are shown in Table S5. It can be seen that the Mössbauer spectra of FeN_x/C-5-700 has little change, which confirms the stability of FeN_x/C-5-700. But FeN_x/C-5-800 changes obviously, and it is severely oxidized to form Fe_3O_4,[18] which may be due to the instability of the exposed Fe/Fe_3C nanoparticles of FeN_x/C-5-800 without the graphene protection (Figure S7).

Control experiments without catalysts or visible light were carried out, exhibiting a very low methane conversion rate (Figure S8), indicating that catalysts and light irradiation are essential for this methane conversion. There are no products observed for the control experiments only without the addition of CH_4, indicating that the products are not derived from the catalyst itself (Figure S8). Isotope labelling experiment of $^{13}CH_4$ was further conducted with FeN_x/C-5-700. In the mass spectra, the peak at $m/z = 48$ can be observed (Figure S9a), which could be attributed to $^{13}CH_3{}^{13}CH_2OH$ (Calcd for $^{13}C_2H_6O$ ($[M]^+$): m/z 48. Found: m/z 48.). Similarly, the peak at $m/z = 47$ was observed (Figure S9b), which indicates the generation of $H^{13}COOH$ (Calcd for $^{13}CH_2O_2$ ($[M]^+$): m/z 47. Found: m/z 47.). These results confirm that the products are derived from CH_4 rather than the catalyst.

The UV-vis absorption spectra of FeN_x/C-5-T shows that these catalysts have good adsorption in the whole UV-vis range (Figure S10). Photocatalytic methane conversion experiments were performed under different monochromatic light irradiation (350, 400, 450, 500, 550, 600 and 650 nm) (Figure S11) to calculate the apparent quantum efficiency (AQE). For HCOOH production, AQE of FeN_x/C-5-700 at 500 nm was calculated at 2.76 % with the best methane conversion activity.

It is well known that H_2O_2 can be decomposed into $^{\bullet}OH$ with high oxidation ability through Photo-Fenton reaction pathway, but it cannot be ignored that H_2O_2 can also be decomposed into O_2 and H_2O, then subsequently may convert to $^{\bullet}O^{2-}$, $^1O_2$ or other reactive oxygen species with less oxidation ability.[19] In order to determine the role of H_2O_2 in methane conversion, formic acid as the main product was taken as an example to compare the catalysis performance, and $^{\bullet}OH$ quencher (Isopropyl alcohol, IPA),[20] $^{\bullet}O^{2-}$ quencher (p-Benzoquinone, PBQ)[21] and $^1O_2$ quencher (2,2,6,6-Tetramethylpiperidine, TEMP)[19b] were selected and added to the methane conversion system catalyzed by FeN_x/C-5-700 under experimental conditions (Figure 4a). It can be easily seen that IPA can sharply reduce the yield of formic acid from 4659 to 504 μmol g_{cat}^{-1}, which means that $^{\bullet}OH$ from the H_2O_2 decomposition plays a decisive role for the methane conversion.

In order to evaluate the degree of H_2O_2 decomposition, the H_2O_2 reduction potentials of FeN_x/C-5-T were measured on glassy carbon rotating ring-disk electrodes (Figure 4b). FeN_x/C-5-800 show the most negative onset potential of H_2O_2 reduction, indicating that it is much easier to decompose H_2O_2 than those of FeN_x/C-5-700 and FeN_x/C-5-600. But it doesn't seem to be consistent with the photocatalytic results. The abilities to generate $^{\bullet}OH$ from H_2O_2 were further studied through the coumarin fluorescence test, wherein coumarin can selectively react with $^{\bullet}OH$ in solution and form the strong fluorescent substance 7-hydroxycoumarin with a PL signal at around 456 nm.[22] The solution of coumarin and H_2O_2 photocatalyzed by FeN_x/C-5-700 shows the strongest fluorescence emission, the next is FeN_x/C-5-800, and the last one is FeN_x/C-5-600 (Figure 4c). It indicates that FeN_x/C-5-700 has the strongest ability to generate $^{\bullet}OH$, consistent with the photocatalytic results. Electron paramagnetic resonance (EPR) experiments were used to further confirm the $^{\bullet}OH$ generation (Figure 4d). The signal with the intensity ratio of 1:2:2:1 is observed, which could be attributed to $^{\bullet}OH$.[23] And the signal intensity increases as prolonging the light irradiation time, which is consistent with the coumarin fluorescence test (Figure S12). It indicates that the light can promote the $^{\bullet}OH$ generation, and it is Photo-Fenton like reaction. Associated with the degree of H_2O_2 decomposition by these catalysts, it is speculated that there is another way to compete with the $^{\bullet}OH$ generation, especially for FeN_x/C-5-800. Then,

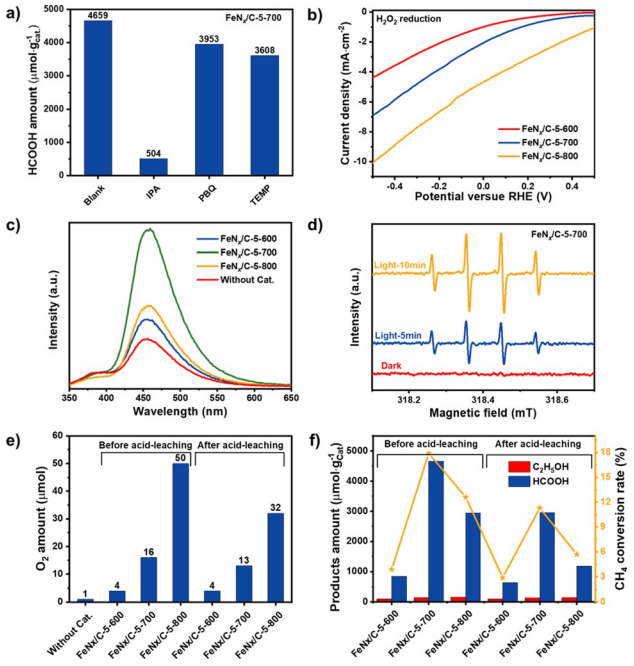

Figure 4. a) Formic acid production by FeN_x/C-5-700 with different quenchers. b) Voltammograms recorded with glassy carbon rotating disk electrodes surface-coated with FeN_x/C-5-T in 0.1 M H_2O_2 and 0.1 M Na_2SO_4 aqueous solution. c) The ·OH-trapping PL spectra of suspensions containing FeN_x/C-5-T/H_2O_2 (0.1 M) and coumarin. d) EPR spectra of DMPO-trapped FeN_x/C-5-T and an H_2O_2-aqueous system under light irradiation. e) Oxygen evolution of as-prepared and acid-leached FeN_x/C-5-T in 0.1 M H_2O_2. f) Yields of liquid products and methane conversion rates of as-prepared and acid-leached FeN_x/C-5-T.

the O_2 evolution in the above system was carried out (Figure 4e). FeN_x/C-5-800 has the highest oxygen evolution (50 μmol), while FeN_x/C-5-700 has only 16 μmol O_2 evolution (Video in SI), suppressing 68% O_2 generation. From the aspect of the product generation, gain factor is another evaluating criterion for the efficiency of H_2O_2 utilization (Table S7). Compared with FeN_x/C-5-800 (Gain factor = 0.23), the gain factor of FeN_x/C-5-700 comes to 0.58. This result is consistent with that of O_2 evolution, and it also reveal that O_2 evolution is main way for the H_2O_2 waste.

In order to confirm the active sites, control experiments with $FeCl_2$ (9 μmol, the same Fe amount of FeN_x/C-5-700, Figure S8) instead of FeN_x/C-5-T was added into the catalytic system, but there is almost no catalytic effect, indicating that the active sites for this reaction are Fe-N_x and/or Fe/Fe_3C rather than Fe ions. In addition, after simply mixing the FeN_x/C-5-600 and FeN_x/C-5-800, the catalytic reaction was carried out, and the catalytic effect is less than FeN_x/C-5-700 (Figure S8), indicating that there is a synergistic effect between Fe-N_x and Fe/Fe_3C. Taking into account the catalytic activity (Figure 3 and Figure 4) and structure of these three catalysts (Table S5), it is speculated that Fe-N_x, especially for the low spin state, is the active site for ·OH generation. The proper amount of Fe/Fe_3C nanoparticles, especially for Fe_3C species, may promote the catalysis process.[24]

To further support the above speculation, two control experiments were carried out. Firstly, SCN^- can coordinate with Fe-N_x sites and poison them, so KSCN was added into the photooxidation methane reaction system.[25] The methane conversion rate and formic acid yield of FeN_x/C-5-700 decreases significantly to only 2% and 540 μmol g_{cat}^{-1}, respectively (Figure S13), which can be attributed to the poison of Fe-N_x sites by KSCN. Secondly, FeN_x/C-5-T were soaked in 2 M HCl at 60 °C for 3 h to remove or substantially diminish Fe/Fe_3C nanocrystals rather than Fe-N_x sites. The XPS image and XRD image in Figure S14 confirms that almost no Fe/Fe_3C nanoparticles were found after the acid leaching. Then the experiment of oxygen evolution was carried out. As shown in Figure 4e, after leaching these three catalysts with acid, the amount of oxygen evolution of FeN_x/C-5-600 is unchanged, FeN_x/C-5-700 decreases slightly and FeN_x/C-5-800 decreases significantly. In addition, the experiment of methane conversion was also carried out. As shown in Figure 4f, the methane conversion rate of FeN_x/C-5-600 decreases slightly after leached with acid, but FeN_x/C-5-700 and FeN_x/C-5-800 decrease significantly to 11% and 6%, respectively. Compared with FeN_x/C-5-600, FeN_x/C-5-700 has less Fe-N_x active sites (Table S5), but it still shows higher catalytic performance than that of FeN_x/C-5-600 after acid leaching. Thus, Fe-N_x at the low spin state is more important for the catalysis. Associated with the analysis of Fe_3C and Fe^0 (Table S5), it is speculated that Fe/Fe_3C nanoparticles (FeN_x/C-5-700), especially for Fe_3C, boost Fe-N_x to produce ·OH for methane conversion, while Fe/Fe_3C nanoparticles (FeN_x/C-5-800) with more Fe^0 promote O_2 evolution and reduce the H_2O_2 utilization efficiency.

Density functional theory (DFT) calculations were used to further understand the mechanism for the competing reactions of H_2O_2 decomposition. Four possible models with various active sites of FeN_x/C-5-T are determined in Figure S15. H_2O_2 molecules can be easily absorbed on the active Fe-N_x sites to form Fe-OOH, then ·OH can be generated by the homolytic cleavage of FeO-OH.[26] Therefore, the adsorption configurations (Figure S15) and the corresponding dissociation Gibbs free energies (eV) of the reaction intermediate OOH* (ΔG_{OOH}) were studied (Table S9). As for FeN_x/C-5-700, ΔG_{OOH} of Fe-N_x (1.985 eV) is lower than that of Fe^0 (3.306 eV), indicating that FeN_x is more suitable as an active site to decompose Fe-OOH. The ΔG_{OOH} of FeN_x/C-5-800 (1.137 eV) and FeN_x/C-5-700 (1.985 eV) is lower than that of FeN_x/C-5-600 (2.440 eV), indicating that Fe/Fe_3C can reduce ΔG_{OOH} value of FeN_x/C-5-700 and FeN_x/C-5-800 and easily decompose Fe-OOH. In addition, ·OOH can also be ionized into O_2^- through electron transfer process, then the formed ·OOH/O_2^- are prone to reacting with ·OH/H_2O_2 to produce O_2.[27] For the central Fe atom of Fe-N_x, the Bader charges of FeN_x/C-5-800 (7.221) with more Fe atom is higher than that of FeN_x/C-5-700 (7.152) with less Fe atom. It indicates that Fe/Fe_3C nanoparticles of FeN_x/C-5-800 (Fe^0 as the main component) provide more electrons to its Fe-N_4 active sites, which promote the decomposition of H_2O_2 into O_2 instead of useful ·OH. Therefore, Fe/Fe_3C (FeN_x/C-5-700, Fe_3C as the main component) with proper electron is essential for the efficient utilization of H_2O_2.

It is interesting that the main product from this methane conversion system is formic acid instead of methanol. In order to verify the reaction mechanism of methane activation, the process of methane activation to generate methyl radicals in the reaction was first tested by EPR (Figure S16). The signal of methyl radicals was clearly observed after 5 mins light irradiation, and the signal is enhanced as prolonging the irradiation time.[28] In situ infrared (IR) of FeN_x/C-5-700 show that two distinct IR bands attributed to the adsorption of methane molecules on the catalyst can be observed at 3009 and 1295 cm^{-1} (Figure S17),[29] shifting toward lower wavenumbers than that of free methane molecules (3020 and 1306 cm^{-1}). It indicates that FeN_x/C-5-700 can adsorb methane, which benefits to activate methane. Associated with the EPR (Figure 4d) and the coumarin fluorescence test (Figure S12), FeN_x/C-5-700 with the assistant of light irradiation can catalyze the homolytic cleavage H_2O_2 to produce $^{\bullet}OH$ (Photo-Fenton like reaction),[30] which can easily attack C–H bond of methane absorbed on FeN_x/C-5-700 and form $^{\bullet}CH_3$. Then the generated $^{\bullet}CH_3$ and $^{\bullet}OH$ can produce methanol and other deep oxidation or conversion products (e.g. formic acid and ethanol).[8,29] Actually, formic acid is the major product, and ethanol is the minor product without the generation of deeper oxidized product (acetic acid). It indicates that methanol is the major intermediate product. But in the actual reaction, the methanol content is extremely low because methanol may be further oxidized as an intermediate product to produce formic acid and ethanol, and it is much easier than methane oxidation. A series of experiments were carried out to verify the conjecture. 250 μL methanol was added into the methane conversion system, and a significant increase of formic acid and ethanol was observed (Table S10). In addition, introducing 250 μL methanol into the system without methane, and formic acid and ethanol were observed in the products. For the hypothetic mechanism for photocatalytic methane conversion is shown in Figure S18.[31] Therefore, the efficient utilization of H_2O_2 promote the further conversion of intermediate methanol into formic acid.

Conclusion

In summary, the model catalysts containing Fe-N_x sites and Fe/Fe_3C nanoparticles with various contents of Fe^0 and Fe_3C, were carefully analyzed from multiple aspects including the distinguish of Fe species and the active sites, as well as their functions on the H_2O_2 competitive conversion and the methane conversion pathway. This systematic study revealed that Fe/Fe_3C nanoparticles, especially for Fe_3C with proper electron can boost the activity of Fe-N_x in the competitive decomposition of H_2O_2 into $^{\bullet}OH$, overwhelming O_2 generation for further methane conversion. The methane conversion rate is 18% and the liquid oxygenates selectivity is over 96% (formic acid selectivity over 90%, 4659 μmol g_{cat}^{-1}). This study shows an in-depth understanding of the influence of active sites on competitive H_2O_2 conversion, providing guidelines for the efficient H_2O_2 use on the selective oxidation reaction.

Acknowledgements

We thank Prof. Min Jiang (Hangzhou Normal University), Prof. Bo Jiang (Qingdao University of Technology), and Dr. Hui Ning, Dr. Qingshan Zhao, Dr. Yang Wang, and Dr. Wengang Xu (China University of Petroleum) for useful discussions and suggestions. This work was financially supported by NSFC (51672309, 51172285 and 51372277) and the Fundamental Research Funds for Central Universities (18CX07009A). We also acknowledge the Young Taishan Scholars program of Shandong province (tsqn20182027) and technological leading scholar of 10000 talent project (W03020508).

Conflict of interest

The authors declare no conflict of interest.

Keywords: hydrogen peroxide · iron · methane oxygenation · nanomaterials · photochemistry

[1] a) K. Sato, M. Aoki, R. Noyori, *Science* **1998**, *281*, 1646; b) D. Deng, X. Chen, L. Yu, X. Wu, Q. Liu, Y. Liu, H. Yang, H. Tian, Y. Hu, P. Du, R. Si, J. Wang, X. Cui, H. Li, J. Xiao, T. Xu, J. Deng, F. Yang, P. N. Duchesne, P. Zhang, J. Zhou, L. Sun, J. Li, X. Pan, X. Bao, *Sci. Adv.* **2015**, *1*, e1500462; c) Y. Pan, Y. Chen, K. Wu, Z. Chen, S. Liu, X. Cao, W.-C. Cheong, T. Meng, J. Luo, L. Zheng, C. Liu, D. Wang, Q. Peng, J. Li, C. Chen, *Nat. Commun.* **2019**, *10*, 4290; d) H. Hou, X. Zeng, X. Zhang, *Angew. Chem. Int. Ed.* **2020**, *59*, 17356–17376; *Angew. Chem.* **2020**, *132*, 17508–17529; e) A. Maldotti, C. Bartocci, R. Amadelli, E. Polo, P. Battioni, D. Mansuy, *J. Chem. Soc. Chem. Commun.* **1991**, 1487–1489; f) E.-Y. Jeong, M. B. Ansari, S.-E. Park, *ACS Catal.* **2011**, *1*, 855–863.

[2] a) L. Shi, L. Yang, H. Zhang, K. Chang, G. Zhao, T. Kako, J. Ye, *Appl. Catal. B* **2018**, *224*, 60–68; b) L. Wang, P. Jin, S. Duan, J. Huang, H. She, Q. Wang, T. An, *Environ. Sci. Nano* **2019**, *6*, 2652–2661.

[3] a) P. Schwach, X. Pan, X. Bao, *Chem. Rev.* **2017**, *117*, 8497–8520; b) E. McFarland, *Science* **2012**, *338*, 340.

[4] a) M. Ravi, M. Ranocchiari, J. A. van Bokhoven, *Angew. Chem. Int. Ed.* **2017**, *56*, 16464–16483; *Angew. Chem.* **2017**, *129*, 16684–16704; b) P. Tang, Q. Zhu, Z. Wu, D. Ma, *Energy Environ. Sci.* **2014**, *7*, 2580–2591.

[5] a) J. H. Lunsford, *Angew. Chem. Int. Ed. Engl.* **1995**, *34*, 970–980; *Angew. Chem.* **1995**, *107*, 1059–1070; b) C.-G. Zhan, J. A. Nichols, D. A. Dixon, *J. Phys. Chem. A* **2003**, *107*, 4184–4195; c) R. D. Amos, *Mol. Phys.* **1979**, *38*, 33–45.

[6] M. Ahlquist, R. J. Nielsen, R. A. Periana, W. A. Goddard III, *J. Am. Chem. Soc.* **2009**, *131*, 17110–17115.

[7] N. Agarwal, S. J. Freakley, R. U. McVicker, S. M. Althahban, N. Dimitratos, Q. He, D. J. Morgan, R. L. Jenkins, D. J. Willock, S. H. Taylor, C. J. Kiely, G. J. Hutchings, *Science* **2017**, *358*, 223.

[8] X. Cui, H. Li, Y. Wang, Y. Hu, L. Hua, H. Li, X. Han, Q. Liu, F. Yang, L. He, X. Chen, Q. Li, J. Xiao, D. Deng, X. Bao, *Chem* **2018**, *4*, 1902–1910.

[9] J. Deng, D. Deng, X. Bao, *Adv. Mater.* **2017**, *29*, 1606967.

[10] A. Serov, K. Artyushkova, P. Atanassov, *Adv. Energy Mater.* **2014**, *4*, 1301735.

[11] R. Cao, R. Thapa, H. Kim, X. Xu, M. G. Kim, Q. Li, N. Park, M. Liu, J. Cho, *Nat. Commun.* **2013**, *4*, 2076.

[12] J. Liu, E. Li, M. Ruan, P. Song, W. J. C. Xu, *Catalysts* **2015**, *5*, 1167–1192.

[13] G. Wu, K. L. More, C. M. Johnston, P. Zelenay, *Science* **2011**, *332*, 443.
[14] U. I. Kramm, L. Ni, S. Wagner, *Adv. Mater.* **2019**, *31*, 1805623.
[15] J. Li, S. Ghoshal, W. Liang, M.-T. Sougrati, F. Jaouen, B. Halevi, S. McKinney, G. McCool, C. Ma, X. Yuan, Z.-F. Ma, S. Mukerjee, Q. Jia, *Energy Environ. Sci.* **2016**, *9*, 2418 – 2432.
[16] U. I. Koslowski, I. Abs-Wurmbach, S. Fiechter, P. Bogdanoff, *J. Phys. Chem. C* **2008**, *112*, 15356 – 15366.
[17] a) J. Xie, R. Jin, A. Li, Y. Bi, Q. Ruan, Y. Deng, Y. Zhang, S. Yao, G. Sankar, D. Ma, J. Tang, *Nat. Catal.* **2018**, *1*, 889 – 896; b) Y. Kwon, T. Y. Kim, G. Kwon, J. Yi, H. Lee, *J. Am. Chem. Soc.* **2017**, *139*, 17694 – 17699; c) Q. Shen, C. Cao, R. Huang, L. Zhu, X. Zhou, Q. Zhang, L. Gu, W. Song, *Angew. Chem. Int. Ed.* **2020**, *59*, 1216 – 1219; *Angew. Chem.* **2020**, *132*, 1232 – 1235.
[18] a) R. S. Hargrove, W. Kündig, *Solid State Commun.* **1970**, *8*, 303 – 308; b) F. J. Berry, S. Skinner, M. F. Thomas, *J. Phys. Condens. Matter* **1998**, *10*, 215 – 220.
[19] a) Y. Nosaka, A. Y. Nosaka, *Chem. Rev.* **2017**, *117*, 11302 – 11336; b) M. C. DeRosa, R. J. Crutchley, *Coord. Chem. Rev.* **2002**, *233 – 234*, 351 – 371.
[20] J. D. Rush, W. H. Koppenol, *J. Biol. Chem.* **1986**, *261*, 6730 – 6733.
[21] M. Hayyan, M. A. Hashim, I. M. AlNashef, *Chem. Rev.* **2016**, *116*, 3029 – 3085.
[22] Q. Xiang, J. Yu, P. K. Wong, *J. Colloid Interface Sci.* **2011**, *357*, 163 – 167.
[23] D. Dvoranová, Z. Barbieriková, V. J. M. Brezová, *Molecules* **2014**, *19*, 17279 – 17304.
[24] a) W.-J. Jiang, L. Gu, L. Li, Y. Zhang, X. Zhang, L.-J. Zhang, J.-Q. Wang, J.-S. Hu, Z. Wei, L.-J. Wan, *J. Am. Chem. Soc.* **2016**, *138*, 3570 – 3578; b) X. Ao, W. Zhang, Z. Li, J.-G. Li, L. Soule, X. Huang, W.-H. Chiang, H. M. Chen, C. Wang, M. Liu, X. C. Zeng, *ACS Nano* **2019**, *13*, 11853 – 11862.
[25] Q. Wang, Z.-Y. Zhou, Y.-J. Lai, Y. You, J.-G. Liu, X.-L. Wu, E. Terefe, C. Chen, L. Song, M. Rauf, N. Tian, S.-G. Sun, *J. Am. Chem. Soc.* **2014**, *136*, 10882 – 10885.
[26] a) J. Chen, A. Draksharapu, D. Angelone, D. Unjaroen, S. K. Padamati, R. Hage, M. Swart, C. Duboc, W. R. Browne, *ACS Catal.* **2018**, *8*, 9665 – 9674; b) K. Cheaib, M. Q. E. Mubarak, K. Sénéchal-David, C. Herrero, R. Guillot, M. Clémancey, J.-M. Latour, S. P. de Visser, J.-P. Mahy, F. Banse, F. Avenier, *Angew. Chem. Int. Ed.* **2019**, *58*, 854 – 858; *Angew. Chem.* **2019**, *131*, 864 – 868.
[27] a) W. P. Kwan, B. M. Voelker, *Environ. Sci. Technol.* **2002**, *36*, 1467 – 1476; b) G. C. Taylor, R. J. Waddington, R. Moseley, K. R. Williams, G. Embery, *Biomaterials* **1996**, *17*, 1313 – 1319; c) D. W. McKee, *J. Catal.* **1969**, *14*, 355 – 364.
[28] M. H. Ab Rahim, M. M. Forde, R. L. Jenkins, C. Hammond, Q. He, N. Dimitratos, J. A. Lopez-Sanchez, A. F. Carley, S. H. Taylor, D. J. Willock, D. M. Murphy, C. J. Kiely, G. J. Hutchings, *Angew. Chem. Int. Ed.* **2013**, *52*, 1280 – 1284; *Angew. Chem.* **2013**, *125*, 1318 – 1322.
[29] Y. Zhou, L. Zhang, W. Wang, *Nat. Commun.* **2019**, *10*, 506.
[30] S. Gligorovski, R. Strekowski, S. Barbati, D. Vione, *Chem. Rev.* **2015**, *115*, 13051 – 13092.
[31] Q. Xing, *Basic Organic Chemistry*, *Vol. 4*, 4th ed., Peking University Press, Peking, **2016**, pp. 113 – 135.

Manuscript received: December 20, 2020
Revised manuscript received: January 21, 2021
Accepted manuscript online: February 4, 2021
Version of record online: March 10, 2021

